Depth profile reconstructions of electronic transport properties in H^+ MeV-energy ion-implanted n-Si wafers using photocarrier radiometry

Rui Tai,[1] Chinhua Wang,[1,a)] Jingpei Hu,[1] and Andreas Mandelis[2]
[1]*Institute of Modern Optical Technologies & Collaborative Innovation Center of Suzhou Nano Science and Technology, Jiangsu Key Lab of Advanced Optical Manufacturing Technologies & MOE Key Lab of Modern Optical Technologies, Soochow University, Suzhou 215006, China*
[2]*Center for Advanced Diffusion-Wave Technologies, Department of Mechanical and Industrial Engineering, University of Toronto, Ontario M5S 3G8, Canada*

(Received 18 May 2014; accepted 24 June 2014; published online 18 July 2014)

A depth profiling technique using photocarrier radiometry (PCR) is demonstrated and used for the reconstruction of continuously varying electronic transport properties (carrier lifetime and electronic diffusivity) in the interim region between the ion residence layer and the bulk crystalline layer in H^+ implanted semiconductor wafers with high implantation energies (~MeV). This defect-rich region, which is normally assumed to be part of the homogeneous "substrate" in all existing two- and three-layer models, was sliced into many virtual thin layers along the depth direction so that the continuously and monotonically variable electronic properties across its thickness can be considered uniform within each virtual layer. The depth profile reconstruction of both carrier life time and diffusivity in H^+ implanted wafers with several implantation doses (3×10^{14}, 3×10^{15}, and $3\times10^{16}\,cm^{-2}$) and different implantation energies (from 0.75 to 2.0 MeV) is presented. This all-optical PCR method provides a fast non-destructive way of characterizing sub-surface process-induced electronic defect profiles in devices under fabrication at any intermediate stage before final metallization and possibly lead to process correction and optimization well before electrical testing and defect diagnosis becomes possible. © *2014 AIP Publishing LLC*. [http://dx.doi.org/10.1063/1.4887117]

I. INTRODUCTION

Accurate control and evaluation of the electronic properties of ion implanted semiconductors have been an important issue in the electronics industry.[1–3] During the ion implantation process, semiconductors are electronically compromised due to the interaction of implanted ions and the crystalline structure, which forms an inhomogeneous structure with depth-varying subsurface electronic properties. To investigate the properties of the ion-implanted samples, photothermal radiometry (PTR) has been used to characterize the electronic behavior via infrared thermal photon emission which is related to non-radiative de-excitation processes.[4–6] On the other hand, frequency-domain photocarrier radiometry (PCR) is a dynamic modulated photoluminescence technique directly related to radiative de-excitation processes. It was found to be a sensitive method for characterization and subsurface defect imaging of semiconductor materials.[7] There have been several theoretical and experimental studies for the PCR response of ion-implanted inhomogeneous semiconductors.[8–11] Li *et al.*[10] developed a three-layer theoretical model to characterize low-energy (up to ~100 keV) ion-implanted semiconductors in which a uniform surface layer (~100-nm thick), a uniform ion-implanted layer (~100-nm below the surface layer), and a uniform intact substrate layer are assumed. When the implantation energy increases (e.g., to MeV level), the implanted ions traverse increasingly deeper surface layers and reside at a considerable depth (~tens of μm), spread over a narrow region (~2–3 μm) adjacent to the crystalline substrate. Based on the physics of deep ion implantation, Wang *et al.*[11] developed a two-layer theoretical PCR model in which the thin ion residence layer is considered to be an interface that separates the surface layer and the assumed uniform substrate. While those models can well explain the PCR signal dependence on ion implantation dose, all reports so far have considered the ion-implanted sample as two or three "effective" layers in which the ion traversed region, the eventual ion residence region and the substrate were assumed to be "uniform." In reality, in two- and three-layer models the region beneath the ion residence layer, i.e., the "substrate" is inhomogeneous within a certain distance, e.g., tens of μm, from the ion accumulation depth due to diffusion of excess ions and implant-ion-generated defect densities emanating from that depth. From this point of view, all "effective" PCR models are relatively inaccurate although they can qualitatively explain phenomena observed in ion-implanted samples. To reconstruct the depth profile of the ion implanted samples, Salnick and Mandelis[5] and Othonos *et al.*[6] developed an inverse-problem algorithm using Hamiltonian plasma-harmonic oscillator theory to characterize the depth profile of low-energy implanted (~tens of KeV) silicon with the PTR technique. Due to the complicated algorithm involved in the PTR approach which requires the measurement of a large number of both thermal and optoelectronic parameters of semiconductors, it may be difficult to ascertain the uniqueness of the inverse problem reconstruction. In this paper, we propose

a)Author to whom correspondence should be addressed. Electronic mail: chinhua.wang@suda.edu.cn.

and demonstrate a PCR forward fitting method which involves only a few optoelectronic parameters and is thus more suitable for high-fidelity inverse-problem reconstructions of transport properties in ion-implanted semiconductors, specifically of high-energy ion implantation in the MeV regime. The depth profiles of both lifetimes and carrier diffusivities are reconstructed based on a new theoretical-computational method and the effectiveness of the method is validated through the experimental data of different H^+ implanted wafers.

II. THEORETICAL MODEL

High-energy implanted ions traverse the surface layer of a semiconductor down to a depth of tens of micrometers (in contrast to ~tens of nm at low implantation energies) and reside in a narrow region to form an "effective" interface which is further followed by an electronically inhomogeneous layer beneath the ion residence layer due to ion diffusion and/or defect-compromised lattice integrity. The electronic properties of the diffused inhomogeneous layer vary monotonically with depth up to tens of micrometers thick, depending on the implantation energy and eventually saturate to the intact substrate. Fig. 1(a) shows the configuration of a high-energy ion-implanted wafer. The ion traversed region (on the order of tens of μm) at the top of the implanted wafer that is actually "defect saturated", is assumed to be uniform. The ion residence region (~2–3 μm wide) is assumed to be an equivalent interface at $L = L_1$. Below the interface, the layer is inhomogeneous within a depth of tens of μm. Fig. 1(b) schematically shows the behavior of the major electronic transport properties (carrier lifetime and carrier diffusivity) varying with depth in the case of high-energy ion implanted wafers. The properties remain constant in the ion-traversed layer because of the statistical uniformity of the saturated defects. In the diffused inhomogeneous layer, the electrical transport properties (D and τ) increase monotonically as the damage degree decreases along the depth until their values saturate in the intact substrate. There is a physical interface between the traversed and the inhomogeneous layer within which discontinuous electronic properties between the two regions occur. To calculate the contributions to the overall PCR signal from different layers of the structure including the traversed layer and the inhomogeneous layer, the inhomogeneous layer is sliced into many virtual sub-layers along the depth direction so that each sub-layer can be considered uniform. The final PCR signal is then obtained as a superposition of contributions from the traversed layer and each virtual sub-layer.

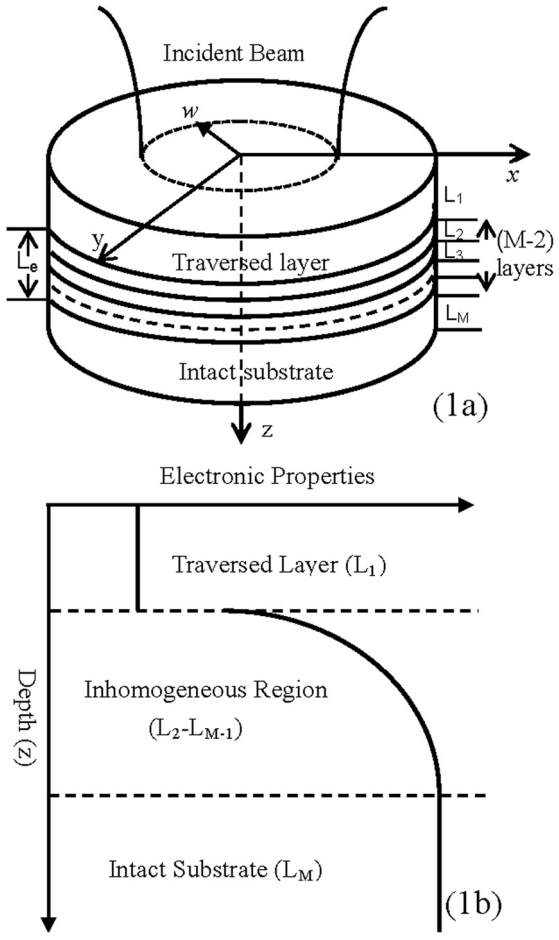

FIG. 1. (a) Configuration of a high-energy ion-implanted inhomogeneous semiconductor structure and (b) the depth profiles of electronic properties in this structure.

In Fig. 1(a), the thickness of each virtual layer slice is denoted by $L_j (j = 1,2,\ldots M)$, in which L_1 is the ion traversed layer, L_M is the intact substrate, and L_2 to L_{M-1} are the actual inhomogeneous layers. L_e is the depth of the inhomogeneous region separating the ion traversed region and the intact substrate, which can be expressed by $L_e = \sum_{j=2}^{M-1} L_j$. The exciting laser beam is assumed to be of finite size with a Gaussian profile, $\exp(-r^2/w^2)$, where w is the radius of the laser beam spot size.

The optically injected three-dimensional carrier densities $N_j(r,z,\omega)$ $(j = 1,2,\ldots M$ stands for each elementary virtual layer) can be calculated from the carrier transport equations:

$$\nabla^2 N_j(r,z,\omega) - \sigma_j^2 N_j(r,z,\omega) = -\frac{G_j(r,z,\omega)}{D_j}, \quad j = 1,2,\ldots,M. \tag{1}$$

Here D_j is the carrier diffusivity for each layer. The complex plasma-wave vector σ_j is defined as:

$$\sigma_j = \sqrt{\frac{1 + i\omega\tau_j}{D_j\tau_j}}, \tag{2}$$

where τ_j is the carrier lifetime of each layer. G_j is the source term given by the following expressions:

For the first (uppermost surface) ion-traversed layer, $j = 1$,

$$G_1(r,z,\omega) = \frac{\alpha_1(1-R_1)P\eta}{\pi w^2 h\nu}\exp\left(-\frac{r^2}{w^2} - \alpha_1 z\right). \tag{3a}$$

For other layers, $2 \le j \le M$,

$$G_j(r,z,\omega) = \frac{\alpha_1 P\eta}{\pi w^2 hv}\prod_{n=1}^{j}(1-R_n) \times \exp\left(-\frac{r^2}{w^2} - \sum_{n=1}^{j-1}\alpha_n L_n - \alpha_j\left(z - \sum_{n=1}^{j-1} L_n\right)\right). \quad (3b)$$

Here α_j is the absorption coefficient of each layer. P and hv are the power and the photon energy of the incident radiation, respectively, and η is the optical-to-electronic conversion quantum efficiency. R_n is the reflectivity at each subsurface, of which only the reflectivity at the equivalent interface (R_1) has a real value while those at other virtual sliced layers are all equal to zero. The boundary conditions for the carrier density wave at the front and the rear surface of the wafer are:

$$D_1\frac{\partial N_1(r,z,\omega)}{\partial z} = s_1 N_1(r,z,\omega), \quad z=0, \quad (4a)$$

$$D_M\frac{\partial N_M(r,z,\omega)}{\partial z} = -s_{M+1}N_M(r,z,\omega), \quad z = L_1+L_2+\cdots+L_M. \quad (4b)$$

s_1 and s_M are the effective recombination velocities at the front and rear surface of the wafer, respectively. The boundary conditions for the carrier wave at other interfaces ($j=2\ldots M$) are

$$N_{j-1}(r,z,\omega) = N_j(r,z,\omega), z = L_1+L_2+\cdots+L_{j-1}, \quad (4c)$$

$$D_{j-1}\frac{\partial N_{j-1}(r,z,\omega)}{\partial z} = D_j\frac{\partial N_j(r,z,\omega)}{\partial z} - s_j N_j(r,z,\omega), \quad z = L_1+\cdots+L_{j-1}. \quad (4d)$$

Here s_j is the effective recombination velocity at each interface, in which only the recombination velocity (s_2) at $L=L_1$ (equivalent interface) is nonzero while recombination velocities at all other virtual interfaces (s_3-s_M) are equal to zero. The Hankel transform method was used to solve the equation after taking into account the cylindrical symmetry of the boundary-value problem. By taking the Hankel transforms of the carrier transport equation, Eq. (1), we obtain:

$$\frac{d^2\tilde{N}_j(\lambda,\omega,z)}{dz^2} - \beta_j^2\tilde{N}_j(\lambda,\omega,z) = -\frac{\tilde{E}_j\exp\left(z-\sum_{n=1}^{j-1}L_n\right)}{D_j}, \quad (5)$$

where λ is the Hankel variable and β_j is defined as: $\beta_j = \sqrt{\sigma_j^2+\lambda^2}$.[9] The numerator at the right side of Eq. (5), $\tilde{E}_j\exp(z-\sum_{n=1}^{j-1}L_n)$, stands for the Hankel transform of the source term G_j in Eq. (1):

for $j=1$,

$$\tilde{E}_1 = \frac{\alpha_1(1-R)\eta P}{2\pi hvD_1}\frac{\exp\left(-\frac{\sigma^2 w^2}{4}\right)}{{\beta_1}^2-{\alpha_1}^2}, \quad (6a)$$

for $2\le j\le M$,

$$\tilde{E}_j = \frac{\alpha_j\eta P\prod_{n=1}^{j}(1-R_n)}{2\pi hvD_j}\frac{\exp\left(-\frac{{\sigma_j}^2w^2}{4}-\sum_{n=1}^{j-1}\alpha_n L_n\right)}{{\beta_j}^2-{\alpha_j}^2}. \quad (6b)$$

The Hankel transforms of the boundary conditions Eqs. (4a)–(4d), can be expressed as follows:

$$D_1\frac{d\tilde{N}_1(\lambda,z,\omega)}{dz} = s_1\tilde{N}_1(\lambda,z,\omega), z=0, \quad (7a)$$

$$D_M\frac{d\tilde{N}_M(\lambda,z,\omega)}{dz} = -s_{M+1}\tilde{N}_M(\lambda,z,\omega), \quad z = L_1+L_2+\cdots+L_M, \quad (7b)$$

$$\tilde{N}_{j-1}(\lambda,z,\omega) = \tilde{N}_j(\lambda,z,\omega), \quad z = L_1+L_2+\cdots+L_{j-1}, \quad (7c)$$

$$D_{j-1}\frac{d\tilde{N}_{j-1}(\lambda,z,\omega)}{dz} = D_j\frac{d\tilde{N}_j(\lambda,z,\omega)}{dz} - s_j\tilde{N}_j(\lambda,z,\omega), \quad z = L_1+L_2+\cdots+L_{j-1}. \quad (7d)$$

The free-carrier densities in Hankel space can be solved from Eq. (5):

$$\tilde{N}_j(\lambda,z,\omega) = \tilde{A}_j\exp\left[-\beta_j\left(z-\sum_{n=1}^{j-1}L_n\right)\right] + \tilde{B}_j\exp\left[\beta_j\left(z-\sum_{n=1}^{j-1}L_n\right)\right] + \tilde{E}_j\exp\left[-\alpha_j\left(z-\sum_{n=1}^{j-1}L_n\right)\right], \quad j=1,\ldots,M. \quad (8)$$

A recursion relation of coefficients $\tilde{A}_j$ and $\tilde{B}_j$ in Eq. (8) for adjacent layers can be derived from the boundary conditions:

$$\begin{bmatrix}\tilde{A}_j\\ \tilde{B}_j\end{bmatrix} = \begin{bmatrix}t_{11}^{j-1} & t_{12}^{j-1}\\ t_{21}^{j-1} & t_{22}^{j-1}\end{bmatrix}\begin{bmatrix}\tilde{A}_{j-1}\\ \tilde{B}_{j-1}\end{bmatrix} + \begin{bmatrix}c_1^{j-1}\\ c_2^{j-1}\end{bmatrix}. \quad (9)$$

The detailed analytical expressions for the coefficients t_{mn}^j and c_m^j ($m, n=1, 2$) in the transform matrix are as follows:

$$t_{11}^{j-1} = \left(1+\frac{D_{j-1}\beta_{j-1}-s_j}{D_j\beta_j}\right)\exp\left(-\beta_{j-1}L_{j-1}\right), \quad (10a)$$

$$t_{12}^{j-1} = \left(1-\frac{D_{j-1}\beta_{j-1}+s_j}{D_j\beta_j}\right)\exp\left(\beta_{j-1}L_{j-1}\right), \quad (10b)$$

$$t_{21}^{j-1} = \left(1-\frac{D_{j-1}\beta_{j-1}-s_j}{D_j\beta_j}\right)\exp\left(-\beta_{j-1}L_{j-1}\right), \quad (10c)$$

$$t_{22}^{j-1} = \left(1-\frac{D_{j-1}\beta_{j-1}+s_j}{D_j\beta_j}\right)\exp\left(\beta_{j-1}L_{j-1}\right), \quad (10d)$$

$$c_1^{j-1} = \left(1 + \frac{D_{j-1}\alpha_{j-1} - s_j}{D_j\beta_j}\right)\tilde{E}_{j-1}\exp(-\alpha_{j-1}L_{j-1}) - \tilde{E}_j\left(1 + \frac{\alpha_j}{\beta_j}\right), \tag{10e}$$

$$c_2^{j-1} = \left(1 - \frac{D_{j-1}\alpha_{j-1} - s_j}{D_j\beta_j}\right)\tilde{E}_{j-1}\exp(-\alpha_{j-1}L_{j-1}) - \tilde{E}_j\left(1 - \frac{\alpha_j}{\beta_j}\right). \tag{10f}$$

The relationship between an arbitrary virtual layer and the first layer can be deduced using the above recursion relation Eq. (9):

$$\begin{bmatrix}\tilde{A}_K\\ \tilde{B}_K\end{bmatrix} = \begin{bmatrix}t_{11}^{K-1} & t_{12}^{K-1}\\ t_{21}^{K-1} & t_{22}^{K-1}\end{bmatrix}\cdots\begin{bmatrix}t_{11}^{1} & t_{12}^{1}\\ t_{21}^{1} & t_{22}^{1}\end{bmatrix}\begin{bmatrix}\tilde{A}_1\\ \tilde{B}_1\end{bmatrix} + \begin{bmatrix}t_{11}^{K-1} & t_{12}^{K-1}\\ t_{21}^{K-1} & t_{22}^{K-1}\end{bmatrix}\cdots\begin{bmatrix}t_{11}^{2} & t_{12}^{2}\\ t_{21}^{2} & t_{22}^{2}\end{bmatrix}\begin{bmatrix}c_1^{1}\\ c_2^{1}\end{bmatrix} + \ldots + \begin{bmatrix}t_{11}^{K-1} & t_{12}^{K-1}\\ t_{21}^{K-1} & t_{22}^{K-1}\end{bmatrix}\begin{bmatrix}c_1^{K-2}\\ c_2^{K-2}\end{bmatrix} + \begin{bmatrix}c_1^{K-1}\\ c_2^{K-1}\end{bmatrix} \quad K = 2,\ldots,M. \tag{11a}$$

The relations for the last layer (intact substrate layer) and the first layer (traversed layer) can be written as:

$$\begin{bmatrix}\tilde{A}_M\\ \tilde{B}_M\end{bmatrix} = \begin{bmatrix}t_{11}^{M-1} & t_{12}^{M-1}\\ t_{21}^{M-1} & t_{22}^{M-1}\end{bmatrix}\cdots\begin{bmatrix}t_{11}^{1} & t_{12}^{1}\\ t_{21}^{1} & t_{22}^{1}\end{bmatrix}\begin{bmatrix}\tilde{A}_1\\ \tilde{B}_1\end{bmatrix} + \begin{bmatrix}t_{11}^{M-1} & t_{12}^{M-1}\\ t_{21}^{M-1} & t_{22}^{M-1}\end{bmatrix}\cdots\begin{bmatrix}t_{11}^{2} & t_{12}^{2}\\ t_{21}^{2} & t_{22}^{2}\end{bmatrix}\begin{bmatrix}c_1^{1}\\ c_2^{1}\end{bmatrix} + \ldots + \begin{bmatrix}t_{11}^{M-1} & t_{12}^{M-1}\\ t_{21}^{M-1} & t_{22}^{M-1}\end{bmatrix}\begin{bmatrix}c_1^{M-2}\\ c_2^{M-2}\end{bmatrix} + \begin{bmatrix}c_1^{M-1}\\ c_2^{M-1}\end{bmatrix}. \tag{11b}$$

An equation set linking the unknown coefficients $\tilde{A}_1, \tilde{B}_1, \tilde{A}_M, \tilde{B}_M$ is thus obtained from two equations generated from the above matrix, Eq. (11b), and the boundary conditions in Hankel space Eqs. (7a) and (7b). The coefficients $\tilde{A}_1, \tilde{B}_1, \tilde{A}_M, \tilde{B}_M$ are obtained by solving the equation set through computer programming. The coefficients of all the other layers can be obtained using Eq. (11a) after $\tilde{A}_1$ and $\tilde{B}_1$ are determined. The final signal in Hankel space can be expressed as a summation of the contributions from all the layers:

$$\tilde{S}_{PCR}(\omega) = \int_0^{L_1}\tilde{N}_1(\lambda, z, \omega)dz + \sum_{j=2}^{M}\int_{L_1+\ldots+L_{j-1}}^{L_1+\ldots+L_j}\tilde{N}_j(\lambda, z, \omega)dz. \tag{12}$$

Taking into the account, the collection efficiency of the detector, the final PCR signal to be detected is thus obtained by taking the inverse Hankel transform of Eq. (12) and integrating the corresponding results over the effective aperture of the detector which is assumed to be a disk with radius a:

$$S_{PCR}(\omega) = \frac{1}{\pi a}\int_0^{\infty}\tilde{S}_{PCR}(\omega)J_1(\lambda a)d\lambda. \tag{13}$$

Equation (13) represents the PCR signal detected by the IR detector.

III. NUMERICAL SIMULATION

In the theoretical model, the electronic transport properties of each layer must be determined in advance to calculate the final signal. As mentioned above, the electronic transport properties are expected to increase or decrease monotonically in the inhomogeneous region before reaching their saturation value in the intact substrate. Therefore, two formulas were introduced to describe the depth profiles for the carrier lifetime (τ) and carrier diffusivity (D) (Ref. 13) in this region, which feature arbitrary monotonic trends, either increase or decrease, of a property before it reaches a saturation state:

$$K = K_0\left(\frac{1 + \Delta\exp(-qz)}{1 + \Delta}\right)^2, \quad \Delta = \frac{1 - \sqrt{K_\infty/K_0}}{\sqrt{K_\infty/K_0} - \exp(-qL_e)}, \quad K = \tau, D. \tag{14}$$

K_0 and K_∞ represent the initial and saturation values of the carrier lifetime (τ) and carrier diffusivity (D) in the inhomogeneous region, respectively. L_e is the thickness of the inhomogeneous layer; q represents the inhomogeneous electronic transport property gradient. These four parameters together determine the shape of the profile of K. Usually, K_∞, i.e., the saturated value of the carrier life time or carrier diffusivity of the intact substrate is assumed to be known. The remaining three parameters, i.e., q, K_0 and L_e are set as the fitting parameters. Once these parameters, K_0, K_∞, L_e, and q are determined, the electronic transport properties at each layer can be obtained according to the depth profile along z in Eq. (14). In principle, increasing the number of virtual slice layers for the inhomogeneous region (L_e) will decrease the thickness of each layer and increase the calculation accuracy, however, this is offset by the computational complexity and time. To determine a suitable number of sliced layers, an auxiliary simulation was performed. In the simulation, 30 points of the PCR signal vs. modulation frequency were calculated. Since the ion traversed layer should be tens of micrometers thick in the case of high-energy implantation, the thickness of the ion traversed layer (L_1) was assumed to be 10 μm and the optical absorption coefficient of this region was assumed to be $1.2 \times 10^5\,\mathrm{m}^{-1}$. The electronic transport properties of the ion traversed layer and the intact substrate were fixed at 0.4 μs and 0.6 cm^2/s, and 10 μs and 20 cm^2/s, respectively. The front surface carrier recombination velocities (s_1), and those at the equivalent physical interface (s_2) and the rear surface (s_{M+1}) were assumed to be 150, 500, and 0.028 m/s, respectively. The thickness of the inhomogeneous layer (L_e) was assumed to be 100 μm. Fig. 2 shows the amplitude and the phase of the PCR signal varying with frequency in the case of 3, 5, 10, 30, and 50 virtual layers. From the figure, it can be seen that when the number of the sliced layers are 30 or more, the amplitude and phase signals

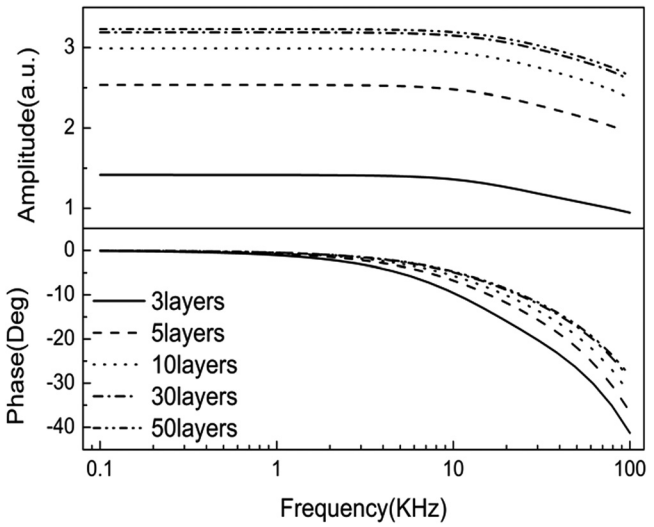

FIG. 2. Amplitude and phase of the PCR signal variation vs. modulation frequency with the number of the virtual sliced layers ranging from 3 to 50. The thickness of the inhomogeneous interlayer is 100 μm.

almost reach saturation and do not change significantly. Therefore, it is found that the number of the sliced layers for the inhomogeneous region (L_e) can be fixed at ~30 to obtain a good balance between accuracy and computational complexity, including time to full computation. Compared with earlier two- and three-layer models, the crucial improvement in the model in this paper is accounting for an inhomogeneous layer below the ion-residence region. To investigate the effect of this layer on the signal, five different thicknesses (L_e) of this inhomogeneous region were assumed: 10, 20, 30, 40, and 50 μm. The carrier recombination velocities of the front surface (s_1), and the equivalent physical interface velocity (s_2) were assumed to be 80 and 250 m/s, respectively. L_1 was assumed to be 5 μm and the optical absorption coefficient of this region was assumed to be $5 \times 10^5\,\mathrm{m}^{-1}$. The electronic transport properties of the ion traversed layer and of the intact substrate were fixed at 0.2 μs and 0.5 cm^2/s, and 10 μs and 20 cm^2/s, respectively. The simulation results are shown in Fig. 3. It is seen that the amplitude and the phase of the PCR signal vary sensitively with the thickness of the inhomogeneous sub-surface region. In the foregoing two simulations, the initial values of the electronic transport properties in the inhomogeneous region are fixed at 2 μs and 5 cm^2/s, respectively. In addition to the thickness of this inhomogeneous layer (L_e), note that the initial values of the electronic properties of this region (τ_0 and D_0) are also important parameters. To thoroughly investigate the effect of the added inhomogeneous region on the final result, the effect of the initial electronic transport properties of this region should also be considered independently. Three groups of the initial electronic properties of the inhomogeneous layer were assumed: 8 μs, 10 cm^2/s; 1 μs, 2 cm^2/s; and 0.2 μs, 0.4 cm^2/s, with the thickness of the ion-traversed layer *(L_1)* and the inhomogeneous layer *(L_e)* being set at 20 μm and 50 μm, respectively. The optical absorption coefficient in L_1 was assumed to be $7 \times 10^4\,\mathrm{m}^{-1}$. The carrier recombination velocities at the front surface (s_1), and at the equivalent physical interface (s_2), were assumed to be 100 and 250 m/s, respectively. The simulation results for these three cases are illustrated in Fig. 4. From the figure, we can see that the effect of the initial electronic properties of the inhomogeneous on the final PCR signal was significant. In all simulations the incident Gaussian laser beam spotsize was assumed to be 800 μm and the effective aperture of the NIR detector was assumed to be 850 μm. The optical absorption coefficients in all other layers were assumed to be $6.6 \times 10^4\,\mathrm{m}^{-1}$.

Those simulations confirmed that the assumed inhomogeneous region below the ion residence layer has a pronounced effect on PCR signal, unlike the homogeneity assumption made in prior two- and three-layer models. Therefore, taking this effect into account in our theoretical model is necessary and justified.

IV. EXPERIMENTAL, RESULTS, AND DISCUSSION

In the experiment, eleven n-Si semiconductor wafers with the same thickness (505 μm) were divided into three

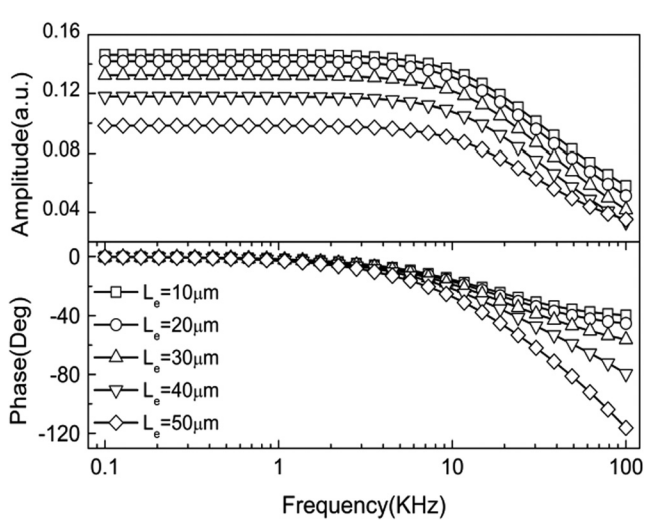

FIG. 3. Amplitude and phase of the PCR signal variation vs. with the modulation frequency for five values of L_e: 10, 20, 30, 40, and 50 μm.

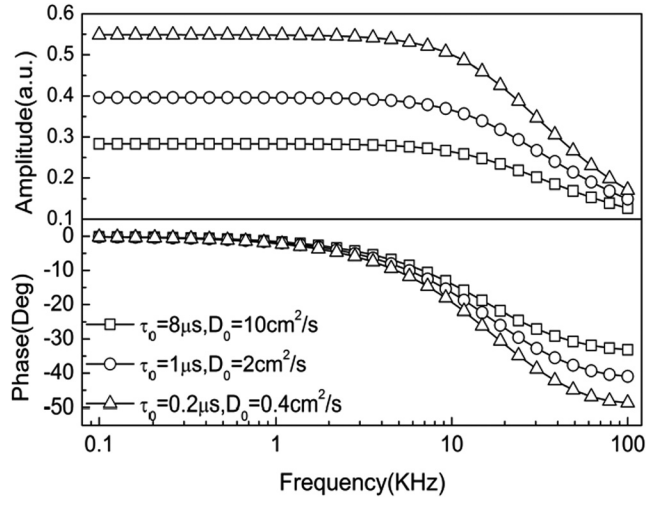

FIG. 4. Amplitude and phase of the PCR signal variation vs. modulation frequency for three sets of values for τ_0 and D_0: 8 μs, 10 cm^2/s; 1 μs, 2 cm^2/s, and 0.2 μs, 0.4 cm^2/s.

sets which were H^+ implanted with a dose of $3 \times 10^{14}\,cm^{-2}$, $3 \times 10^{15}\,cm^{-2}$, and $3 \times 10^{16}\,cm^{-2}$, respectively, and for each set they were implanted at different energies varying from 0.75 to 2.00 MeV. The depth of the region traversed by ions (L_1) can be obtained with the SRIM technique.[14] Fig. 5 shows a typical experimental ion distribution configuration along the depth coordinate with 1.25 MeV implantation energy. The depth values at the central peak are 10.9, 16.6, 23.2, 30.8, and 48.8 μm for wafers with implantation energies of 0.75, 1.00, 1.25, 1.50, and 2.00 MeV, respectively. These values were used as known parameters in the numerical fitting and in the depth profile reconstruction of the two transport parameters for wafers with different implantation energies. The detailed experimental setup has been described elsewhere.[10,11] The laser was operated at 830 nm wavelength and the laser power was 34 mW. The beam size (w) was measured to be approximately 800 μm. The near-IR emission from the sample was collected and focused through a pair of reflective objectives onto an InGaAs detector, preamplifier, and optical cut-on filter assembly. The effective radius of the detector was estimated to be 850 μm and the spectral response range of the detector was 0.8–1.8 μm. The PCR frequency scan was performed from 0.5 to 100 kHz with a total of 31 logarithmically spaced points.

The saturation values of the transport properties (τ_∞ and D_∞) were determined through several non-implanted wafers from the same batch as the three sets of implanted wafers used in the experiment, and the mean values of these parameters were found to be approximately 17.0 μs and 17.5 cm^2/s, respectively. These values served as the transport properties of the intact substrate for all the experimental ion-implanted wafers in the fitting procedure. The optical absorption coefficient of $6.6 \times 10^4\,m^{-1}$ for crystalline silicon wafer at 830 nm (Ref. 15) was used for the region L_2-L_M and this value remains the same for all the experimental wafers. In the fitting process, a parameter C, which represents the ratio of the theoretical value and the voltage output of the experimental system, was determined using a reference semiconductor sample. Then this value was fixed for the other investigated samples. As a result, the relative PCR amplitudes among all the samples reflect meaningful changes in electronic properties of the wafers after implantation. The determination of the parameter C also helps to enhance the accuracy and uniqueness of the fits to data from a series of samples with relative transport property changes. In our measurements, the value of C was found to be 79.05 MKS units. In addition to the front-surface recombination velocity (s_1), the equivalent interface recombination velocity (s_2), the optical absorption coefficient (α_1), the carrier lifetime and diffusivity of the traversed layer (τ_1 and D_1), τ_0, D_0, q and L_e in Eq. (14) were set as the fitting parameters. In the multiparameter fitting process, the following variance between the theory and the experiment was minimized:

$$\text{var} = \sum_{i=1}^{2} \frac{\sum_{j=1}^{N} [P_{i,fit}(f_j) - P_{i,e}(f_j)]^2}{\sum_j [P_{i,e}(f_j)]^2}, \tag{15}$$

where $i = 1, 2$ represent the amplitude and the phase, respectively. N is the total number of data points (31 points in this case). $P_{i,e}$ (f_j) is the experimental PCR amplitude and phase and $P_{i,fit}$ (f_j) is the fitted PCR amplitude and phase calculated with the multi-layer model. The fitting error is defined as the square root of variance in percent (%). In the fitting process, initial values of the fitted parameters, which are given according to the empirical values, were used in a forward calculation to measure the electronic properties of each layer (τ_j and D_j) using Eq. (14). Then the overall PCR signal was obtained through Eq. (13). The variance between the theoretical value and the experimental PCR signal data using Eq. (15) was then calculated and minimized by repeatedly adjusting the values of the fitted parameters. The effects of different parameters of ion implanted semiconductors on the photocarrier radiometry (PCR) signal have been investigated previously,[10,11,16] which show that the effects of different parameters (e.g., lifetime, diffusivity, and surface recombination velocity) on the PCR signal can be well deconvoluted from each other in the physically meaningful range of these parameters. Results also showed[16] that other mathematically possible solutions of the fitted parameters are far beyond the meaningful range of semiconductors physics.

The amplitude and phase behavior of the PCR signal as a function of frequency and the corresponding best-fitted theoretical curves for the three sets of ion-implanted semiconductor wafers are shown in Fig. 6. Very good agreement between the best-fitted curves and the experimental data was obtained with fitting error less than 10%. It can be seen that for each set with the same implantation dose, the amplitude and the phase lag of the PCR signal decreases with implantation energy. The thicker implantation layers at higher energy increase electronic defect densities which impede radiative recombination, enhancing the nonradiative recombination pathway, instead. The phase of each set also shows the same trend as the amplitude, i.e., a decrease with increasing implantation energy. This is due to the deeper damaged layer resulting in diminished participation in the overall PCR signal of free-carrier wave radiative recombination in the intact substrate and a concomitant shift of the mean carrier-wave density centroid[12] toward the surface.

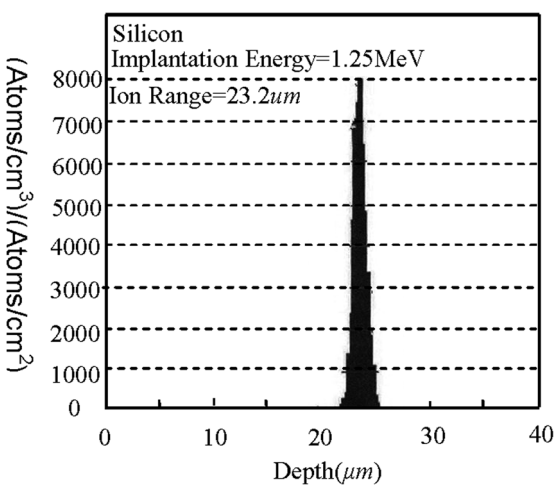

FIG. 5. Typical ion distribution of H^+ implanted silicon at 1.25 MeV implantation energy.

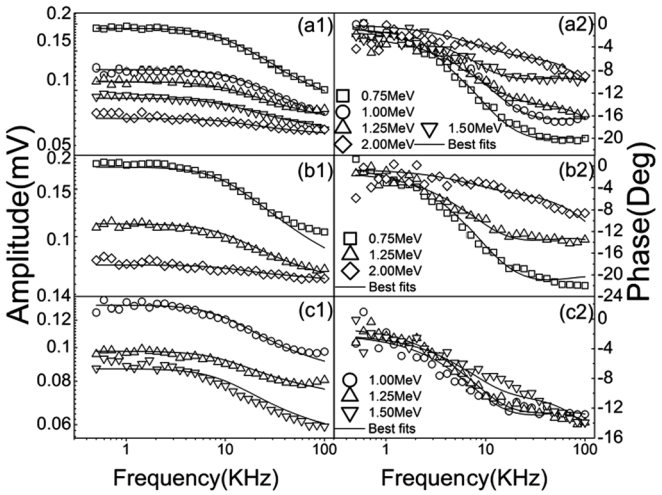

FIG. 6. Experimental frequency dependence of PCR amplitudes and phases, and the corresponding best-fitted theoretical curves for H^+ implanted Si wafers at several implantation energies with *a*, *b*, *c* corresponding to the implantation dose of $3 \times 10^{14}\,cm^{-2}$, $3 \times 10^{15}\,cm^{-2}$, and $3 \times 10^{16}\,cm^{-2}$, respectively.

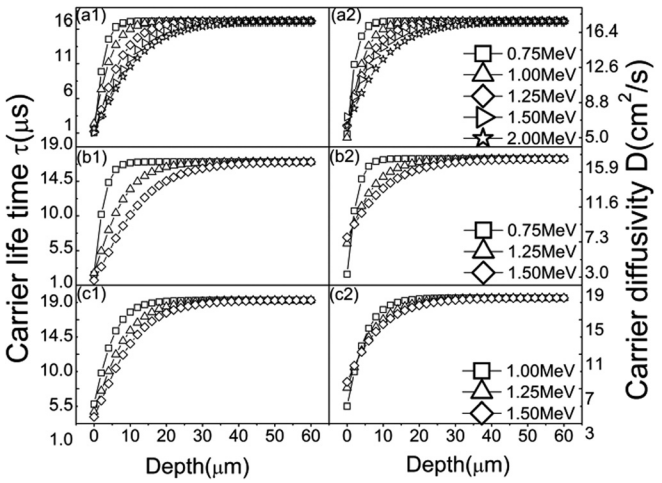

FIG. 7. The reconstructed depth profiles for the carrier diffusivity and the carrier life time for H^+ implanted semiconductor wafers at several implantation energies with *a, b,* and *c* corresponding to the implantation dose of $3 \times 10^{14}\,cm^{-2}$, $3 \times 10^{15}\,cm^{-2}$, and $3 \times 10^{16}\,cm^{-2}$, respectively.

Fig. 7 shows the results of the reconstructed depth profiles of the two electronic transport properties in the inhomogeneous region. This is done by substituting the best-fitted values of electronic transport properties, τ_0 and D_0, L_e and the gradient q into Eq. (14), which generates the profiles of the electronic transport properties in the inhomogeneous region. We can see that the thickness of the inhomogeneous region increases with increasing implantation energy for each set of wafers with the same implantation dose, as expected. The detailed best-fitted results for each PCR-probed wafer are listed in Table I. We can see that the initial value in the depth profiles of the carrier lifetime (τ_0) vary within the range of 1 to 3 μs, while the value of the carrier diffusivity (D_0) lies between 5 and 7 cm^2/s, thereby showing their insensitivity to the increased implantation energy. This is because the depth profile begins just below the ion residence layer, which features similar types and densities of defects caused by the interaction of the implanted ions and the crystalline structure together with the ion-traversed layer. The front-surface recombination velocity s_1 is also insensitive to the increased implantation energy, especially at the higher implantation energies, as expected. When compared with s_1, the interface recombination velocity s_2 decreases considerably with increased implantation energy. This can be qualitatively understood by the fact that higher energies result in increasingly more remote locations for the actual damaged region, which leads to increased crystalline integrity and decreased interface recombination velocity s_2. The carrier lifetime and diffusivity in the ion-traversed layer (τ_1 and D_1) fluctuate in a narrow range for different implantation doses and energies since the crystalline structure in this region reaches to a "saturated" state of defects.

V. CONCLUSIONS

We have introduced a PCR depth profiling technique for the reconstruction of continuously variable carrier lifetimes and electronic diffusivities in H^+ implanted semiconductor wafers with high implantation energy (~MeV). We developed a multi-layer theory and a recursion relation among the virtual layers constituting the inhomogeneous layer. The overall theoretical PCR signal was fitted to the experimental amplitude and phase, and depth profiles of both carrier lifetime and diffusivity for three implantation doses were obtained. This

TABLE I. Best-fitted results for the experimental data using the multi-layer model for three sets of samples with the implantation dose of $3 \times 10^{14}\,cm^{-2}$, $3 \times 10^{15}\,cm^{-2}$, and $3 \times 10^{16}\,cm^{-2}$, respectively, and various implantation energies.

No.	Implanted dose (cm^{-2})	Implanted energy (MeV)	Thickness of L_1 (μm)	Fitted s_1 (m/s)	Fitted s_2 (m/s)	Fitted α_1 (m^{-1})	Fitted τ_0 (μs)	Fitted D_0 (cm^2/s)	Fitted τ_1 (μs)	Fitted D_1 (cm^2/s)	Fitted L_e (μm)	Fitted q (cm^{-1})
1	3×10^{14}	0.75	10.9	15.8	228.5	3.09×10^5	1.1	5.4	0.27	0.86	10.5	5714
2	3×10^{14}	1.00	16.6	7.5	101.1	2.00×10^5	2.4	5.0	0.15	0.30	20.0	3000
3	3×10^{14}	1.25	23.2	5.5	84.5	1.56×10^5	1.2	6.3	0.26	0.53	30.6	1961
4	3×10^{14}	1.50	30.8	5.9	70.0	1.37×10^5	1.1	7.3	0.13	0.51	40.7	1474
5	3×10^{14}	2.00	48.8	6.6	52.0	0.96×10^5	1.7	6.3	0.22	0.52	50.9	1180
6	3×10^{15}	0.75	10.9	16.5	258.2	3.15×10^5	2.4	3.4	0.24	1.11	11.8	5085
7	3×10^{15}	1.25	23.2	7.6	92.2	1.64×10^5	2.6	7.1	0.16	0.55	35.2	1705
8	3×10^{15}	2.00	48.8	8.3	68.5	1.01×10^5	1.7	7.9	0.25	0.51	54.6	1100
9	3×10^{16}	1.00	16.6	8.8	137.7	2.34×10^5	3.5	5.0	0.14	0.21	24.4	2500
10	3×10^{16}	1.25	23.2	6.9	93.2	1.59×10^5	2.6	7.1	0.20	0.33	37.6	1596
11	3×10^{16}	1.50	30.8	6.1	71.0	1.30×10^5	1.9	7.8	0.22	0.33	46.4	1293

inverse method provides a fast nondestructive means for characterizing the sub-surface process-induced electronic defects in devices under any and all stages of fabrication well before electrical testing can be done following end-point metallization. The theoretical model is also suitable for characterizing any implanted semiconductors that contain arbitrary depth profiles of inhomogeneous electronic properties.

ACKNOWLEDGMENTS

This work was supported by a grant from the National Natural Science Foundation of China Contract No. 60877063, Scientific Research Foundation for Returned Scholars, Ministry of Education of China, and the project of the Priority Academic Program Development (PAPD) of Jiangsu Higher Education Institutions. AM gratefully acknowledges the Canada Research Chairs program and the Natural Sciences and Engineering Research Council (NSERC) of Canada for a Discovery Grant. The preparation of the implanted semiconductor wafers from Bernd Burchard and Jan Meijer, RUBION, Ruhr-Universitaet Bochum, Germany was gratefully acknowledged.

[1]X. Liu, B. Li, and Q. Huang, Chin. Phys. B **19**, 097201 (2010).
[2]A. Gutiérreza, M. E. Rodríguez-García, and J. Giraldo, Physica B **406**, 3687 (2011).
[3]L. Qin, J. Y. Liu, and Y. Wang, Appl. Mech. Mater. **268–270**, 1623 (2012).
[4]A. Salnick, A. Mandelis, F. Funak, and C. Jean, Appl. Phys. Lett. **71**, 1531 (1997).
[5]A. Salnick and A. Mandelis, J. Appl. Phys. **80**, 5278 (1996).
[6]A. Othonos, A. Salnick, A. Mandelis, and C. Christofides, Phys. Status Solidi A (RRN) **161**, R13 (1997).
[7]A. Mandelis, J. Batista, and D. Shaughnessy, Phys. Rev. B **67**, 205208 (2003).
[8]J. Batista, A. Mandelis, and D. Shaughnessy, Appl. Phys. Lett. **82**, 4077 (2003).
[9]A. Mandelis, J. Appl. Phys. **97**, 083508 (2005).
[10]B. Li, D. Shaughnessy, A. Mandelis, J. Batista, and J. Garcia, J. Appl. Phys. **95**, 7832 (2004).
[11]C. Wang, A. Mandelis, J. Tolev, B. Burchard, and J. Meijer, J. Appl. Phys. **101**, 123109 (2007).
[12]A. Mandelis, *Diffusion-Wave Fields: Mathematical Methods and Green Functions* (Springer-Verlag, New York, 2001), Chap. 9.
[13]M. Munidasa, F. Funak, and A. Mandelis, J. Appl. Phys. **83**, 3495 (1998).
[14]J. F. Ziegel and J. P. Biersack, see www.srim.org for "SRIM."
[15]*Handbook of Optical Constants of Solids*, edited by E. D. Palik (San Diego, Academic, 1998), Vols. **I** and III.
[16]M. E. Rodriguez, A. Mandelis, G. Pan, L. Nicolaides, J. A. Garcia, and Y. Riopel, J. Electrochem. Soc. **147**(2), 687–698 (2000).